

# Towards reconstructing experimental sparse-view X-ray CT data with diffusion models

Nelas J. Thomsen<sup>\*†</sup>, Xinyuan Wang<sup>†</sup>, Felix Lucka<sup>†</sup>, Ezgi Demircan-Tureyen<sup>†</sup>

<sup>\*</sup>Martin-Luther-University Halle-Wittenberg, Institute of Physics, Halle, Germany

<sup>†</sup>Centrum Wiskunde & Informatica, Computational Imaging Group, Amsterdam, The Netherlands

**Abstract**—Diffusion-based image generators are promising priors for ill-posed inverse problems like sparse-view X-ray Computed Tomography (CT). As most studies consider synthetic data, it is not clear whether training data mismatch (“domain shift”) or forward model mismatch complicate their successful application to experimental data. We measured CT data from a physical phantom resembling the synthetic Shepp-Logan phantom and trained diffusion priors on synthetic image data sets with different degrees of domain shift towards it. Then, we employed the priors in a Decomposed Diffusion Sampling scheme on sparse-view CT data sets with increasing difficulty leading to the experimental data. Our results reveal that domain shift plays a nuanced role: while severe mismatch causes model collapse and hallucinations, diverse priors outperform well-matched but narrow priors. Forward model mismatch pulls the image samples away from the prior manifold, which causes artifacts but can be mitigated with annealed likelihood schedules that also increase computational efficiency. Overall, we demonstrate that performance gains do not immediately translate from synthetic to experimental data, and future development must validate against real-world benchmarks.

**Index Terms**—X-ray Computed Tomography, computational imaging, diffusion priors, image generation.

## I. INTRODUCTION

Diffusion-based image generators are increasingly used in plug-and-play solvers for ill-posed inverse problems such as sparse-view X-ray CT reconstruction. These methods hinge on balancing two competing forces: the prior (what the diffusion model says a typical image should look like) and the likelihood (what the CT measurement data requires the image to be). The interplay between these two components is critical, as excessive reliance on the prior can lead to loss of detail or hallucinations, while overemphasizing data fidelity may amplify artifacts or fail to resolve ambiguities arising from the ill-posedness of the inverse problem.

The balance becomes critical when applying these methods to experimental data, where the gap between model and reality widens. The challenge in the likelihood force arises from the mismatch between the simplified forward model and the physics of the real-world acquisition process. While simulated measurements follow exact mathematical projectors, experimental scans contain geometric inaccuracies, beam hardening, scatter, and complex noise textures that the standard likelihood term often fails to account for. This discrepancy forces the

This work was supported by the Dutch Research Council (NWO, file number VI.Vidi.223.059)

solver to either amplify artifacts when fitting the incorrect data or rely overly on the prior to mask this mismatch.

The challenge in the prior force, on the other hand, stems from the distributional shift between the training data and the experimental target. Standard diffusion models are typically trained on idealized synthetic datasets that lack the specific geometric and textural variations found in physical objects. A prior trained on such narrow, idealized distributions becomes brittle when faced with real-world objects, often failing to reconstruct features that deviate from the training set. Conversely, a prior specialized solely on experimental geometries may lack the generalization capability to handle unseen variations. Thus, achieving robust experimental reconstruction requires not only managing the forward model mismatch but also designing priors that can bridge the gap between the clean synthetic domain and the imperfect experimental domain.

In this work, we examine how the performance of diffusion-based solvers for sparse-view CT translates to real experimental settings. To enable a controlled comparison, we designed a physical phantom that resembles the standard Shepp-Logan phantom, isolating specific sources of error. Our contributions are threefold: First, we analyze the impact of training distribution and demonstrate that while rigid geometric mismatch leads to drastic failure, a diverse prior may offer superior robustness against geometric challenges inherent to real-world objects. Second, we investigate forward model mismatch, showing that it manifests as not only severe streak artifacts, but also as structural misalignments, a specific form of hallucination where the solver distorts features to fit physical inconsistencies. Finally, we address practical inference strategies, demonstrating that an annealed likelihood schedule effectively reconciles the diffusion prior with imperfect experimental measurements even with significantly fewer sampling steps.

## II. RELATED WORKS

### A. Preliminaries on Diffusion Models

Diffusion models [1] generate images by learning to invert a predefined noising process. In denoising diffusion probabilistic models (DDPMs) [1], this inversion is formulated as a Markovian reverse-time process, where each denoising step is modeled as a Gaussian distribution parameterized by a neural network  $\epsilon_\theta$ . The network is trained to predict the noise realization at a given state, which effectively estimates the mean of the reverse conditional distribution. Deterministic sampling schemes like DDIM [2] leverage this to define a

non-Markovian trajectory, allowing for the direct estimation of the clean image  $\hat{\mathbf{x}}_t$  from a noisy observation  $\mathbf{x}_t$  at any timestep. This estimate, often referred to as the Tweedie denoised estimate [3], is given by:

$$\hat{\mathbf{x}}_t := \frac{1}{\sqrt{\bar{\alpha}_t}} \left( \mathbf{x}_t - \sqrt{1 - \bar{\alpha}_t} \epsilon_{\theta^*}^{(t)}(\mathbf{x}_t) \right), \quad (1)$$

where  $\bar{\alpha}_t$  is the noise schedule parameter and  $\epsilon_{\theta}$  is the predicted noise.

### B. Diffusion-based Priors for Tomography

Assuming the tomographic measurement model  $\mathbf{y} = \mathbf{Ax}_0 + \mathbf{n}$ , the goal is to reconstruct the unknown image  $\mathbf{x}_0 \in \mathbb{R}^n$  from projection data  $\mathbf{y} \in \mathbb{R}^m$ , where  $\mathbf{n} \in \mathbb{R}^m$  models measurement noise. Here  $\mathbf{A} : \mathbb{R}^n \rightarrow \mathbb{R}^m$  denotes the known tomography forward operator such as a discretized Radon transform mapping an image to line-integral measurements. By Bayes' Rule, the posterior score (i.e., the gradient of the log-posterior) decomposes as:

$$\nabla_{\mathbf{x}_t} \log p(\mathbf{x} \mid \mathbf{y}) = \nabla_{\mathbf{x}_t} \log p(\mathbf{x}) + \nabla_{\mathbf{x}_t} \log p(\mathbf{y} \mid \mathbf{x}), \quad (2)$$

with the score  $\nabla_{\mathbf{x}_t} \log p(\mathbf{x})$  being approximated by a pre-trained model  $\epsilon_{\theta}(\mathbf{x}_t, t)$ . Thus, posterior sampling can be seen as combining a learned “prior direction”  $\epsilon_{\theta}(\mathbf{x}_t, t)$  with a physics-based “data direction”  $\mathbf{A}^{\top}(\mathbf{y} - \mathbf{Ax})$ , assuming  $\mathbf{n} \sim \mathcal{N}(\mathbf{0}, \sigma_y^2 \mathbf{I})$ . Sampling approaches vary in the way they combine these two directions. Plug-and-play (PnP) approaches operate by injecting a likelihood-guidance term into each reverse diffusion step [4]–[8]. Given the data consistency loss  $\ell(\mathbf{x}) = \frac{1}{2} \|\mathbf{y} - \mathbf{Ax}\|^2$ , the widely used DPS sampler [6] updates the iterate at each reverse diffusion step according to:

$$\mathbf{x}_{t-1} = \sqrt{\bar{\alpha}_{t-1}} (\hat{\mathbf{x}}_t - \gamma_t \nabla_{\mathbf{x}_t} \ell(\hat{\mathbf{x}}_t)) + \tilde{\mathbf{w}}_t(\eta) \quad (3)$$

where  $\gamma_t$  denotes the step size in data direction and  $\tilde{\mathbf{w}}_t(\eta)$  is overall noise term governed by  $\eta \in [0, 1]$ , which interpolates from fully deterministic sampling to fully stochastic ancestral sampling. Decomposed diffusion sampler (DDS) [7] proposed to replace computationally expensive Jacobian term in Eq. (3) with a gradient-based surrogate, converting a step on the noisy generative manifold into a projected step onto the clean image manifold  $\mathcal{M}$ , i.e.,  $\hat{\mathbf{x}}_t - \gamma_t \nabla_{\mathbf{x}_t} \ell(\hat{\mathbf{x}}_t) = \mathcal{P}_{\mathcal{M}}(\hat{\mathbf{x}}_t - \zeta_t \nabla_{\hat{\mathbf{x}}_t} \ell(\hat{\mathbf{x}}_t))$ . This projection is then implemented via an  $M$ -step conjugate gradient (CG), i.e.,  $\text{CG}(\mathbf{A}^{\top} \mathbf{A}, \mathbf{A}^{\top} \mathbf{y}, \hat{\mathbf{x}}_t, M)$ .

### III. METHODOLOGY

In order to realize an experimental scan of an object similar to the standard canonical Shepp-Logan (SL) phantom, we designed a physical phantom by laser-cutting ellipses in a 6mm-thick transparent polymethyl methacrylate (PMMA) plate. Two ellipses were left as air-filled regions, while the remaining ones were filled with deep-pour transparent epoxy resin. The scans were performed using a custom-built laboratory X-ray CT scanner located in the FleX-ray Lab at the CWI in Amsterdam. We acquired 901 equally spaced projections over a full rotation of the sample. The system operated in a cone-beam geometry

TABLE I: Parameters Used for Tailoring Training Sets

Dataset	Center	$\sigma_A$	$\sigma_{a,b}$	$\sigma_{x_0,y_0}$	$\sigma_{\phi}$	$p_{\text{add,drop}}$
$\mathcal{X}_{\text{exp}}$	$E_{\text{exp}}$	0.03	0.02	0.01	$10^{\circ}$	0.01
$\mathcal{X}_{\text{std}}$	$E_{\text{std}}$	0.03	0.02	0.01	$10^{\circ}$	0.01
$\mathcal{X}_{\text{mix}}$	$E_{\text{mix}}^a$	0.03	0.03	0.02	$45^{\circ}$	0.03

$$^a E_{\text{mix}} = \pi E_{\text{exp}} + (1 - \pi) E_{\text{std}}$$

with a source-to-object distance of 234.92 mm and a source-to-detector distance of 400 mm. The X-ray tube was set to 70 kVp and 600  $\mu\text{A}$  with a 30 ms exposure. Projections were recorded with an effective detector pixel size of 0.2992 mm and 478 detector channels per view. Only the central detector row was recorded, resulting in a fan-beam-equivalent sinogram of size 901×478 (views × channels). Dark-field and flat-field references were acquired for correction.

#### A. Training Data

Let a phantom be defined as a set of ellipses  $E = \{e_i\}_{i=1}^m$ , where each ellipse  $e_i := (A_i, a_i, b_i, x_{0,i}, y_{0,i}, \phi_i)$  encodes intensity, semi-axes, center coordinates, and orientation. For each generated phantom, we construct a sampled set  $E$  by perturbing a mean set  $E_{\mu} = \{e_{i,\mu}\}_{i=1}^m$ . Specifically, for each ellipse  $i$  and each parameter  $p \in \{A, a, b, x_0, y_0, \phi\}$ , we sample

$$p_i = p_{i,\mu} + s_p \varepsilon, \quad \varepsilon \sim \mathcal{N}(0, \sigma_p^2),$$

where  $s_p$  is the corresponding scale, i.e.,

$$s_p = \begin{cases} |p_{i,\mu}|, & p \in \{A, a, b\}, \\ \text{image\_width, image\_height}, & p = x_0, p = y_0, \\ 1, & p = \phi. \end{cases}$$

and  $\sigma_p$  is listed in Table I. This way, we have created three training sets, each of which has 10K images:

- *Standard Shepp-Logan dataset ( $\mathcal{X}_{\text{std}}$ )*: For each phantom, we set  $E_{\mu} := E_{\text{std}}$ , where  $E_{\text{std}}$  is the set of ellipses from the standard Shepp-Logan test image, and sample  $E$  by perturbing all ellipses as above.
- *Experimental Shepp-Logan dataset ( $\mathcal{X}_{\text{exp}}$ )*: For each phantom, we set  $E_{\mu} := E_{\text{exp}}$ , where  $E_{\text{exp}}$  is the set of ellipses from our laser-cut experimental SL, and sample  $E$  by perturbing all ellipses as above.
- *Mixed Shepp-Logan dataset ( $\mathcal{X}_{\text{mix}}$ )*: For each phantom, we first sample  $Z \sim \text{Bernoulli}(\pi)$ . If  $Z = 1$ , we set  $E_{\mu} := E_{\text{exp}}$ ; otherwise  $E_{\mu} := E_{\text{std}}$ . We then sample  $E$  by perturbing all ellipses as above. Here  $\pi \in [0, 1]$  controls the fraction of experimental- versus SL-centered samples in the mixed dataset.

#### B. Generative Priors

Given the datasets described above, we train three priors:

- *Standard SL prior ( $\mathbf{f}_{\text{std}}$ )*: A model trained on  $\mathcal{X}_{\text{std}}$ . It represents a narrow distribution centered on the ideal features of the canonical Shepp-Logan phantom.

- *Experimental SL prior ( $f_{\text{exp}}$ )*: A model trained on  $\mathcal{X}_{\text{exp}}$ . It represents a narrow distribution tailored to the specific geometric properties and ellipse parameters of the laser-cut Shepp-Logan phantom.
- *Mixed SL prior ( $f_{\text{mix}}$ )*: A model trained on the  $\mathcal{X}_{\text{mix}}$ . It represents a distribution with broad coverage, encompassing the variability of both the experimental geometry and the standard analytical phantom.

### C. Reconstruction Pipeline

We use DDS as discussed in Section II-B. Starting from random noise, we perform reverse diffusion sampling from a pre-trained diffusion model using OpenAI guided-diffusion codebase<sup>1</sup> for training, which is guided by measurement-based CG steps. To ensure consistency with our real-world acquisition, the forward operator  $\mathbf{A}$  models the fan-beam geometry used in our experimental setup. The number of sparse projections is variable and equally spaced over the angular range  $[0^\circ, 180^\circ]$ . Image size to be reconstructed is 128x128 in most of the experiments, unless otherwise stated. Due to the low resolution setup, we employ a cosine noise schedule, which mitigates the rapid information loss inherent in linear schedules, ensuring the model encounters meaningful image structure across more timesteps. For experiments in Section IV-A and IV-B, we fixed the following parameters: NFE=1000,  $M = 5$ ,  $\eta = 0.85$ ,  $\sigma_y = 10^{-7}$ , and  $\gamma_t = 1$ .

### D. Test domains

- *Simulation from standard SL ( $y_{\text{sim}(\text{std})}$ )*: A synthetic measurement generated from the canonical SL image.
- *Simulation from experimental-design ( $y_{\text{sim}(\text{cad})}$ )*: A simulation generated from the design parameters  $E_{\text{exp}}$  used to laser-cut the physical phantom. It mimics standard SL geometry with piecewise constant regions, but with reduced contrast levels.
- *Simulation from experimental-reconstruction ( $y_{\text{sim}(\text{recon})}$ )*: A simulation generated by forward-projecting a full-view reconstruction of the physical phantom.
- *Experimental measurement ( $y_{\text{exp}}$ )*: Real-world measurements acquired directly from the physical phantom.

## IV. EXPERIMENTAL RESULTS

### A. Impact of Training Distribution

Fig. 1 quantifies reconstruction performance across a representative simulation-to-experimental spectrum. In the idealized  $y_{\text{sim}(\text{std})}$  domain (leftmost panel), the domain-specific  $f_{\text{std}}$  achieves the highest PSNRs as one may expect, while  $f_{\text{mix}}$  incurs a moderate generalization penalty, and  $f_{\text{exp}}$  collapses to baseline levels due to geometric mismatch between the standard SL and experimental laser-cut phantoms. Moving to the second panel, where the test domain ( $y_{\text{sim}(\text{cad})}$ ) now introduces a geometric shift towards the experimental phantom,  $f_{\text{mix}}$  surprisingly outperforms the domain-specific  $f_{\text{exp}}$  around 5 dB when the number of projections are above five. This

effect might be attributed to the contrast difference between phantoms. The experimental phantom's low-contrast geometry presents a more challenging reconstruction problem. Since  $f_{\text{mix}}$  has been trained with an exposure to high-contrast standard phantoms, it might be providing clearer edge-learning signals that transfer to improve boundary preservation. In the final two panels, the “ground-truth” shifts from idealized design phantoms to full-view reconstructions of experimental data, tying the evaluation directly to achievable experimental quality. These panels differ only in the forward model:  $y_{\text{sim}(\text{recon})}$  uses simulated projections from the reconstructed volume, while  $y_{\text{exp}}$  uses real experimental measurements. In both scenarios, the PSNR gap between  $f_{\text{mix}}$  and the domain-specific  $f_{\text{exp}}$  closes for all projection angles. However, a comparison between the two panels reveals a further performance penalty in the fully experimental case ( $y_{\text{exp}}$ ). While trends remain consistent, absolute PSNR values are systematically lower than in the simulated forward model case ( $y_{\text{sim}(\text{recon})}$ ). This additional degradation isolates the impact of non-ideal forward model factors, such as scatter, beam hardening, and detector noise, which are present in real acquisitions but absent when simulating projections.

Since PSNR alone is insufficient to fully characterize reconstruction quality, and may often mask the artifacts and hallucinations, Fig. 2 shows reconstructions from 12 sparse projections across four domains. The baseline reconstructions using the Conjugate Gradient Least Squares (CGLS) confirm the insufficiency of the measurements. While diffusion priors generally recover high-fidelity structures, significant distribution shifts (e.g., applying  $f_{\text{std}}$  to the laser-cut phantom or  $f_{\text{exp}}$  to the standard SL) cause catastrophic failures. In contrast, the mixed prior  $f_{\text{mix}}$  demonstrates robust generalization, successfully reconstructing all domains with performance comparable to specialized priors on their native distributions. Narrow priors ( $f_{\text{std}}$ ,  $f_{\text{exp}}$ ) occasionally retain residual streaks even on in-distribution samples, as the solver struggles to balance strict prior adherence with data consistency. The broader support of  $f_{\text{mix}}$  appears to smooth out these residual streaks, suggesting that a relaxed prior constraint may ease the tension with the likelihood term. This seems to allow the diffusion process to find natural solutions that satisfy the measurements without overfitting to high-frequency inconsistencies.

### B. Impact of Forward Model Mismatch

As indicated before, the divergence in reconstruction performance between  $y_{\text{sim}(\text{recon})}$  and  $y_{\text{exp}}$  can be attributed to forward model mismatch. Fig. 3 illustrates this effect through line profiles taken from the 25th row of the laser-cut phantom, a region containing three fine holes that represent the phantom's highest-frequency details. In the domain of  $y_{\text{sim}(\text{cad})}$ , especially  $f_{\text{mix}}$  accurately track the ground truth. However, when we transition to experimental data, a systematic offset emerges. Crucially, in the fully experimental domain ( $y_{\text{exp}}$ ), the mismatch forces the likelihood term to dominate the sampling process, pulling the trajectory away from the clean prior manifold. This behavior is hallucination-prone, which

<sup>1</sup><https://github.com/openai/guided-diffusion>

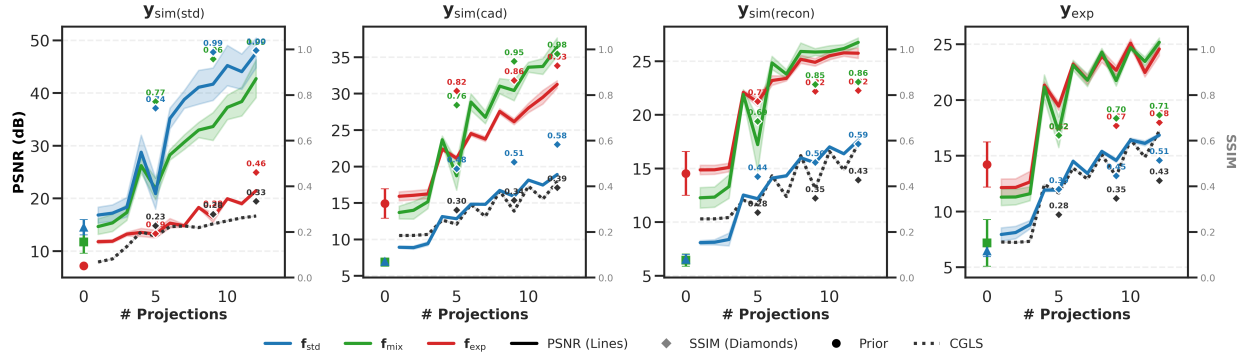


Fig. 1: PSNR (dB) as a function of the number of projections across four different test domains for the reconstructions obtained using CGLS and DDS with three different diffusion priors. Solid lines show PSNR, while diamond markers indicate sampled SSIM values at selected projection counts (5, 9, 12). Shaded areas denote  $\pm 1$  standard deviation across 10 random seeds.

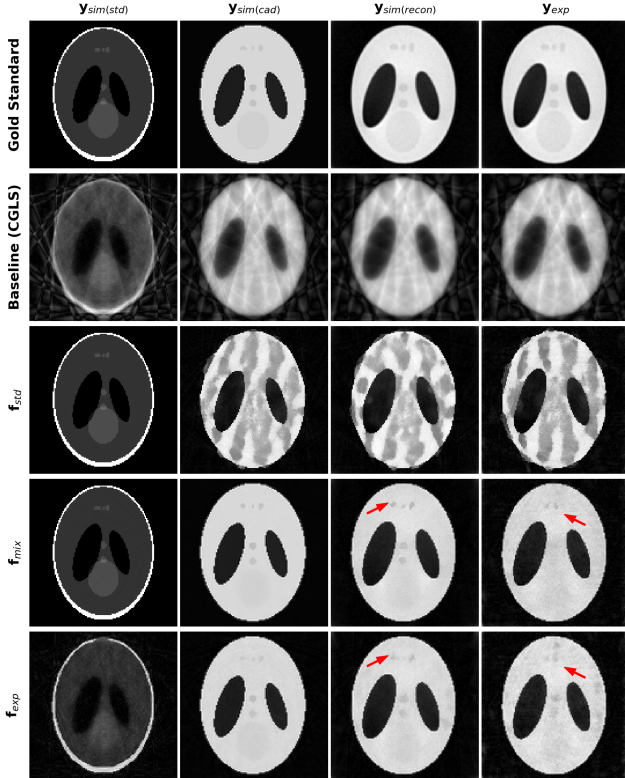


Fig. 2: Example reconstructions using 12 sparse projections across four test domains (rows). From left to right, columns represent: the gold standard, the baseline reconstruction without imposing any prior, reconstructions using standard SL ( $f_{std}$ ), mixed ( $f_{mix}$ ), and experimental SL ( $f_{exp}$ ) diffusion priors.

is manifesting as a spatial shift in the reconstructed profile dips relative to the ground truth. This misalignment suggests that the solver attempts to satisfy the data consistency term not only by propagating artifacts, but by distorting features to align with the physics-mismatched projections.

Since discretization errors typically diminish at finer grids, we investigated whether increasing the reconstruction resolu-

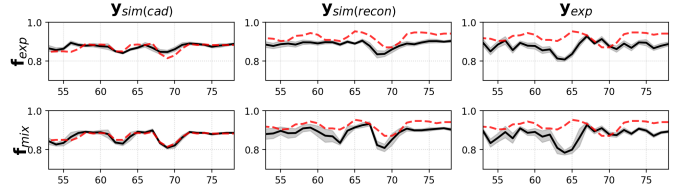


Fig. 3: Line profiles from reconstructions shown in Fig. 2 through the three small holes in the laser-cut phantom. The results involving  $f_{std}$  and/or  $y_{sim(cad)}$  are excluded. Gold standard is represented by red dashed line. Shaded areas show  $\pm 1$  standard deviation across 10 random seeds.

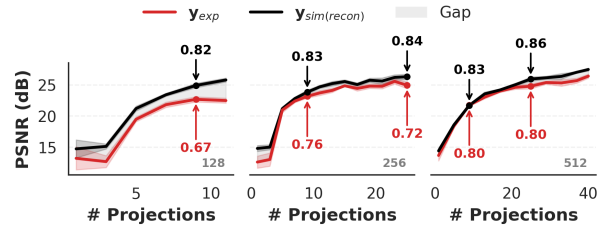


Fig. 4: PSNR (dB) vs number of projections for three resolutions (128, 256, 512) using  $f_{exp}$  on experimental data  $y_{exp}$  and simulated ( $y_{sim(recon)}$ ) reconstructions, revealing the performance gap caused by forward model mismatch. Arrows indicate SSIM values at selected projection counts (9, 25). Shaded bands denote  $\pm 1$  standard deviation.

tion could close the performance gap. Fig. 4 presents reconstruction performance across three resolutions (128, 256, and 512). While the gap between experimental ( $y_{exp}$ ) and simulated ( $y_{sim(recon)}$ ) reconstructions narrows at higher resolutions, a systematic performance deficit persists even at 512x512. This persistent lag confirms that physical model mismatches (e.g., spectral inconsistencies, geometric calibration errors) remain a significant source of error in experimental CT.

TABLE II: Quantitative comparison (PSNR/SSIM) of constant versus linear decay likelihood weight scheduling across different NFEs and view counts.

Schedule	NFE	12 views		24 views	
		PSNR	SSIM	PSNR	SSIM
Constant ( $\gamma = 0.5$ )	1000	24.10	0.7703	25.39	0.7649
	100	22.56	0.7876	23.09	0.7843
	10	19.09	0.7164	20.50	0.7569
Constant ( $\gamma = 5$ )	1000	22.92	0.7367	14.23	0.7295
	100	24.39	0.7267	24.08	0.6977
	10	21.91	0.7134	21.74	0.7079
Linear Decay ( $\gamma_{\max} = 5$ )	1000	23.66	<b>0.8269</b>	24.03	<b>0.8465</b>
	100	23.66	<b>0.8312</b>	<b>24.39</b>	<b>0.8487</b>
	10	22.70	<b>0.7925</b>	<b>23.35</b>	<b>0.8157</b>
Linear Decay ( $\gamma_{\max} = 50$ )	1000	24.85	0.8021	25.03	0.8209
	100	24.19	0.8001	24.14	0.8039
	10	23.00	0.7990	23.11	0.8126
Linear Decay ( $\gamma_{\max} = 150$ )	1000	<b>25.27</b>	0.7801	<b>25.69</b>	0.7817
	100	<b>24.41</b>	0.7757	24.02	0.7693
	10	<b>23.01</b>	0.7891	22.91	0.8033

### C. Impact of Inference Design

The generative prior vs. measured data trade-off in DDS is governed by the number of CG iterations and the likelihood weight ( $\gamma$ ), which is introduced in [7] to modulate the strength of the measurement constraint. This balance is handled within the proximal update step by minimizing the following regularized objective:

$$L(x) = \frac{\gamma}{2} \ell(x) + \frac{1}{2} \|\mathbf{x} - \hat{\mathbf{x}}_t\|_2^2, \quad (4)$$

resulting in  $\text{CG}(\gamma \mathbf{A}^\top \mathbf{A} + \mathbf{I}, \hat{\mathbf{x}}_t + \gamma \mathbf{A}^\top \mathbf{y}, \hat{\mathbf{x}}_t, M)$ . In this,  $\gamma$  serves as a hyperparameter scaling the likelihood relative to the proximity term imposed by the diffusion prior.

In experimental settings, where forward model mismatch is inevitable, a static  $\gamma$  creates a difficult trade-off. Low weight risks hallucination by failing to correct early structural errors, while a high weight forces the model to overfit physical inconsistencies, producing streak artifacts. Our preliminary results in Table II show that at 24 views with NFE=1000, increasing constant  $\gamma$  from 1 to 5 leads to a sharp drop in PSNR (25.33 dB to 14.23 dB), likely due to the amplification of streak artifacts and noise inherent to the mismatch. A scheduling strategy appears to navigate this issue more effectively. By initializing with a high  $\gamma$  during the early, high-noise stages, we can force the trajectory to lock onto the correct global geometry when the prior is weak, while the mismatch errors are already masked by noise. Annealing  $\gamma$  in later stages then relaxes this constraint, allowing the prior to suppress residual artifacts. The results in Table II support this intuition: the linear decay schedule with  $\gamma_{\max} = 150$  is able to achieve best PSNR compared to the constant schedules.

Moving further towards the requirements of real-world experimental CT, we must address another critical challenge beyond physical accuracy: computational feasibility. As we scale to higher resolutions or volumetric (3D) acquisitions,

the computational demand of iterative reconstruction becomes a major bottleneck. While the previous experiments utilized the full denoising chain (NFE=1000) to establish a performance upper bound and to ensure stability, such a heavy computational budget is often impractical for experimental workflows. A key strength of DDS-like sampling schemes is their potential to maintain high reconstruction quality even with a drastically reduced sampling steps. The results in Table II suggest that this efficiency is attainable. When the sampling budget is reduced to NFE=100, the scheduled approach not only remains stable but achieves the highest SSIM across all configurations (0.8487 at 24 views), slightly outperforming even its NFE=1000 counterpart. However, we must also note a critical “sweet spot” regarding these metrics. Visual inspection suggests that while PSNR can mask the retention of streak artifacts, SSIM might hide hallucinations by favoring plausible, piecewise-constant structures. Consequently, despite the slightly lower numerical peaks, the intermediate schedule ( $\gamma_{\max} = 50$ ) likely yields the most robust result in Table II.

## V. CONCLUSION

We have demonstrated that while diffusion-based solvers achieve excellent reconstruction quality on idealized synthetic data, their performance degrades significantly when transitioning to experimental settings. This transition introduces multiple layers of complexity, ranging from geometric challenges in the real-world object to physical inaccuracies in the measurement process. Our controlled study categorizes them into two distinct factors: distributional shift in the prior and physical mismatch in the forward model. Regarding the prior, we find that the best results were obtained for the high-contrast standard SL phantom using a narrowly tailored prior model. Increasing the difficulty with a low-contrast design phantom led to a general decrease in reconstruction quality. Counterintuitively, however, a diverse prior model with a broader support outperformed the specialized prior on this design phantom, suggesting that exposure to varied geometries aids even when the target domain is specific. A further layer of domain shift was introduced via full-view reconstruction of the experimental data, which, unlike the design phantom, no longer exhibit piecewise-constant regions. Crucially, the further performance drop occurs when transitioning to real experimental measurements, as they introduce an additional physics mismatch in the forward operator. This mismatch creates a trade-off where standard constant likelihood weighting leads to either artifact amplification or structural hallucination. To address this, alongside the challenge of computational feasibility, we show that an annealing linear likelihood weight schedule outperforms constant weighting. This relies on the idea of prioritizing data consistency in early, high-noise stages and transitioning to prior dominance as the noise clears. Notably, the preliminary findings suggest that such scheduled inference at reduced sampling steps can yield reconstruction quality comparable to, or even exceeding, that of exhaustive sampling regimes, offering a practical path toward robust experimental application.

## REFERENCES

- [1] J. Ho, A. Jain, and P. Abbeel, “Denoising diffusion probabilistic models,” *Advances in neural information processing systems*, vol. 33, pp. 6840–6851, 2020.
- [2] J. Song, C. Meng, and S. Ermon, “Denoising diffusion implicit models,” *arXiv preprint arXiv:2010.02502*, 2020.
- [3] B. Efron, “Tweedie’s formula and selection bias,” *Journal of the American Statistical Association*, vol. 106, no. 496, pp. 1602–1614, 2011.
- [4] Y. Song, L. Shen, L. Xing, and S. Ermon, “Solving inverse problems in medical imaging with score-based generative models,” in *International Conference on Learning Representations*, 2022.
- [5] H. Chung, B. Sim, D. Ryu, and J. C. Ye, “Improving diffusion models for inverse problems using manifold constraints,” in *36th Conference on Neural Information Processing Systems, NeurIPS 2022*. Neural information processing systems foundation, 2022.
- [6] H. Chung, J. Kim, M. T. Mccann, M. L. Klasky, and J. C. Ye, “Diffusion posterior sampling for general noisy inverse problems,” in *The Eleventh International Conference on Learning Representations*, 2023.
- [7] H. Chung, S. Lee, and J. C. Ye, “Decomposed diffusion sampler for accelerating large-scale inverse problems,” in *12th International Conference on Learning Representations, ICLR 2024*, 2024.
- [8] B. Zhang, W. Chu, J. Berner, C. Meng, A. Anandkumar, and Y. Song, “Improving diffusion inverse problem solving with decoupled noise annealing,” in *Proceedings of the Computer Vision and Pattern Recognition Conference*, 2025, pp. 20895–20905.